Influence of the Foaming Process on the Burning Behavior of the PET−PEN Copolymer

Dong Hyeon Kim, Byeong Jun Lee,* and Byung Kyu Park*

Cite This: ACS Omega 2023, 8, 19556−19566

Read Online

ACCESS | Metrics & More | Article Recommendations

ABSTRACT: The manufacturing process can modify the micromechanical structure, usefulness, and functionality of foams. Although one-step foaming is a simple process, controlling the morphology of the foams is difficult compared to the two-step processing method. In this study, we investigated the experimental differences in thermal and mechanical properties, particularly combustion behavior, between PET−PEN copolymers prepared by the two methods. With an increase in foaming temperature T_f, the PET−PEN copolymers became more fragile, and the breaking stress of the one-step PET−PEN foamed at the highest T_f was only 2.4% of that of the raw material. For the pristine PET−PEN, 24% of the mass was burned, leaving 76% as a molten sphere residue. The two-step MEG PET−PEN had only 1% of its mass remaining as a residue, whereas the one-step PET−PENs had between 41 and 55%. The actual mass burning rates were similar for all the samples except the raw material. The coefficient of thermal expansion of the one-step PET−PEN was about two orders of magnitude lower than that of the two-step SEG.
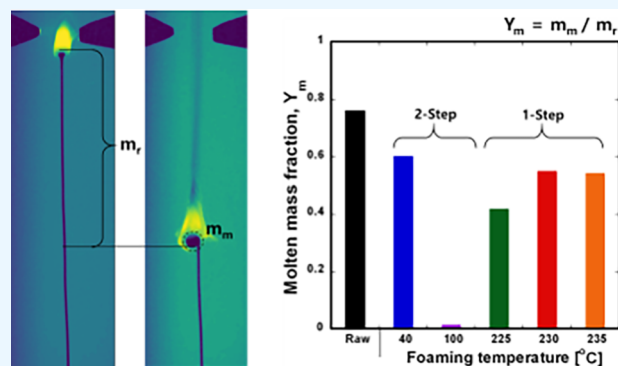
1. INTRODUCTION

The polymer foam expands its applications in the areas of building insulation, aircraft, automobile, and packaging materials through its light weight, high heat resistance, and noise reduction characteristics.[1−6] Recently, it enlarged its uses to thermal energy storage,[7−10] energy harvesting,[11−13] and bioengineering.[14−16]

Understanding the burning behavior of polymers is essential for making informed decisions related to material selection, fire safety, minimizing the environmental impact, and ensuring compliance with regulations.

Polyethylene terephthalate (PET) is one of the most well-known thermoplastic polyester polymers and is used in textiles for clothing and in the manufacture of food containers. Polyethylene naphthalate (PEN) is a polyester used in making high-performance sailcloth and films.[1,17,18] The PET−PEN copolymer has been investigated as an eco-friendly and reusable material.[19] It is suggested to use it as a component of the vacuum insulation panel (VIP) to achieve a net-zero energy house.[20,21]

However, the postfoaming processes of PET−PEN, both one-step and two-step, can affect its thermal conductivity, mechanical compressive stress properties, and combustion characteristics.

The PET−PEN copolymer foam manufacturing process is considered two-step if the saturation process and the foaming process can be separated;[17] otherwise, it is one-step. Figure 1

shows the schematics of the two manufacturing processes. Briefly, the two-step process starts with the pressurizing of the raw material in the vessel of CO_2 to near or above the CO_2 critical pressure. After the CO_2 concentration in the sample has reached the desired value, the pressure is quickly released at a relatively low temperature to prevent the sample from foaming. Then, the sample is immersed in an oil bath at the foaming temperature, T_f, to trigger foaming.[1] This procedure takes up to several days to produce PET−PEN copolymer foams. However, in the one-step process, the sample is directly impregnated with CO_2 at T_f for about an hour. The pressure is then released rapidly at a higher temperature to produce foam cell nucleation and growth.[17,22] The one-step mechanism reduces the manufacturing time through direct foaming.

According to previous research on the two-step PET−PEN copolymer foam, a good correlation exists between the thermal expansion and flame spread rate of PET−PEN microrods.[1] Thermal expansion of the foam is categorized into two distinct groups: the steep expansion group (SEG) and the mild
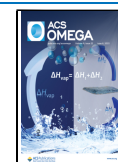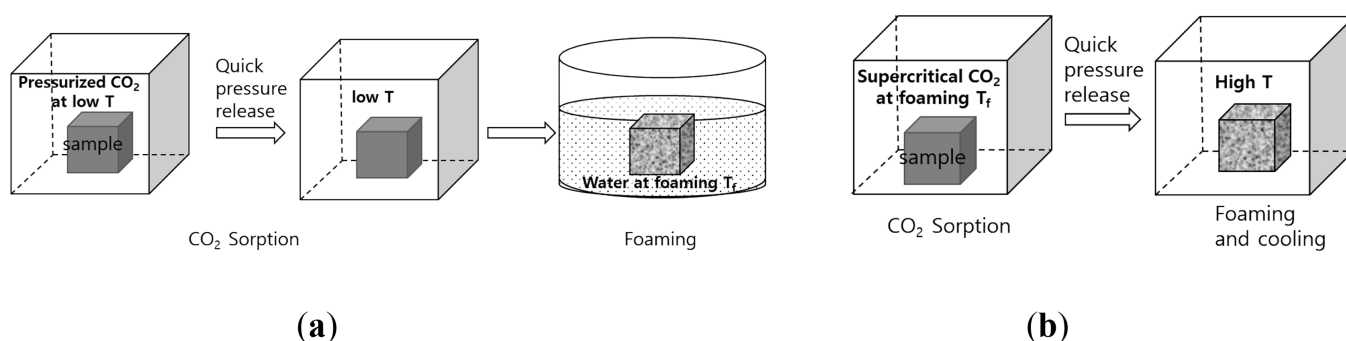
Figure 1. Schematics of the (a) two-step and (b) one-step processes for manufacture of PET–PEN copolymer foam.

expansion group (MEG). Raw and T_f = 40 and 60 °C PET–PEN foams are part of the SEG category, where their length rapidly increases with temperature above the glass transition temperature. In contrast, foaming temperatures of 80 and 100 °C correspond to the MEG group, where the length gradually increases with temperature. The flame spread rate for the SEG cases was approximately 8.5 mm/s, while that for the MEG group was about 3.1 mm/s. These results indicate that each group exhibits comparable thermal expansion and flame spread rate values within their respective categories.

The vacuum insulation panel is a candidate insulating material for zero-energy houses because of its low thermal conductivity.[1] It consists of a core made of glass fiber or polyurethane foam. Recently, the use of PET–PEN as a VIP component material was proposed.[1,20,21] Before PET–PEN can be applied as a housing insulation material, its thermophysical properties, associated safety issues, and combustion characteristics must be pre-evaluated. The objective of this research is to investigate the effects of foaming steps on the flame spread rate, amount of unburned residue, actual burning rate, and mechanical properties of the PET–PEN.

2. MATERIALS AND METHODS

2.1. Materials. A random-type PET–PEN copolymer filament was developed (Kolon Plastics, Kimchun, Korea, reported actual density: 1.33 g/cm³) as an eco-friendly material for kitchens and decoration. Raw PET–PEN (9:1) microrods with a diameter of 0.4 mm were prepared using a 3D printer nozzle. In the additive manufacturing process, the volumetric flow rate was approximately 960 mm³/min at 275 °C.

Two-step PET–PEN copolymer samples with foaming temperatures (T_f) of 40 and 100 °C and one-step samples with T_f of 225 230, and 235 °C were used in the experiments, which are listed in Table 1.

2.2. Methods. *2.2.1. Sample Preparation.* The physical foaming method using CO_2 can be divided into one-step and two-step foaming procedures through a laboratory-scale foaming system. Two-step foaming is favorably adopted due

Table 1. Foaming Temperatures and Their Thermal Expansion Group

	foaming temperature (°C)	thermal expansion group
raw material		steep expansion group
1-step foaming	225, 230, and 235	low expansion group
2-step foaming	40	steep expansion group
	100	mild expansion group

to the precise control of pore distribution. The details of foaming procedures can be found in previous publications.[17,21,22] In this two-step process, however, a long time is required for saturation, roughly up to several days.[22]

To reduce the sorption time, one-step foaming has regained prominence with the development of accurate control devices. The basics of nucleation and cell growth are a single-step process that rapidly releases the pressure from the polymer exposed to CO_2 at a high temperature and pressure. The foaming process was conducted as follows. CO_2 was fed to a 23 cc vessel that contained the PET–PEN filament rolled around a flat jig. The injected CO_2 was then weighed on a scale. The weight of CO_2 was calculated from the density and temperature of CO_2 at the experiment conditions. The CO_2 density was found from the NIST Table. The vessel was then immersed in a salt bath of the specified temperature for 30 min, and then, the pressure was released in less than a second. The vessel was quenched in a water basket. The prepared PET–PEN foam out of the vessel was dried in a temperature-controlled oven.

2.2.2. Measurement of Pore Number Density and Distribution. To visualize the cross-sectional foam structure, samples were cryo-fractured in a glass bath filled with liquid nitrogen using a sharp blade attached to the linear slide mechanism. The prepared samples were coated with ~25 nm-thick platinum using sputtering equipment. A field emission scanning electron microscope (FE-SEM, SUPRA 55VP model) typically with a 2.0 kV acceleration voltage was used to get surface images.

The pore size in the SEM images was measured and analyzed using open ImageJ software and the MorphLibJ libraries to characterize the morphology of the prepared pores. The effective pore diameter, d_{pore}, was calculated from the measured cross-sectional area while assuming a circular geometry.

The cell number density, N_{pore}, i.e., the number of cells per volume of the foam, can be evaluated from the following equation (eq 1):

$$N_{pore} = \left(\frac{n}{A}\right)^{3/2}\left(\frac{1}{C_r}\right)$$

(1)

where n is the number of cells in the probe volume, C_r is the density correction, and A is the interrogation area.

2.2.3. Differential Scanning Calorimetry. For thermal characterization, one and a half cycle tests were performed for the foamed samples using differential scanning calorimetry (Model Discovery, TA Instruments) based on the American Society for Testing and Materials (ASTM) standards (D3417-

83 and D3418-82). To determine the polymer condition prior to one-step foaming, the heat flow history was measured.

Thermal analysis was conducted on the one-step foamed microrods using differential scanning calorimetry in an argon environment. The first cycle was completed by first heating the sample from 30 to 300 °C at a rate of 5 °C/min, holding it at 300 °C for 30 min, and then cooling it to 30 °C at the same rate. The second cycle was repeated in an identical manner after the sample had reached a sufficiently stabilized condition.

To investigate further the weight ratio of the organic components and the thermal stability at a high temperature, the degree of thermal decomposition was measured using a simultaneous differential scanning calorimeter and thermogravimetric (SDT) analyzer (TA Instruments). The derivative weights of the specimens were measured for the temperature range of 30−600 °C at a heating rate of 10 °C/min under an argon atmosphere. As the experiment was similar to that of ref 1, it is explained only briefly here.

2.2.4. Thermal Expansion Measurement. As the temperature increases beyond the glass transition temperature, polymers turn from a solid state to a low viscous amorphous state.[1] To analyze the thermal expansion of PET−PEN, a PET−PEN rod of nominal d = 0.5 mm and 60 mm long was put in a hollow tube of ID = 4 mm, where hot oil was fed through a passage between the outer surface of this tube and a 12.8 mm tube, as shown in Figure 2. Each end of the rod was
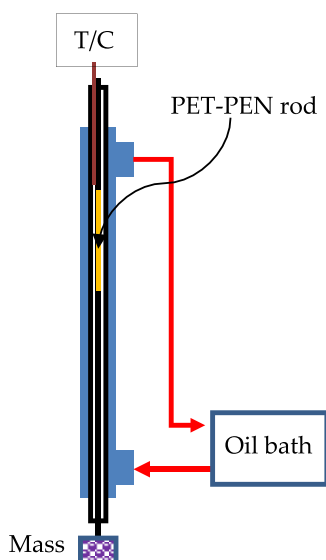

Figure 2. Schematic of the thermal expansion experimental device.

tied to the copper wire, and a 92 g weight was attached to the lower end of the wire to stretch it out. The tube temperature was controlled from 55 to 140 °C by the oil from the circulating bath. With analysis of the recorded video images, i.e., the moving length of the weight, the thermal expansion was measured as a function of time according to ref 1.

2.2.5. Flame Spread Rate Measurement. A 50 mm-long PET−PEN rod was used to obtain the flame spread rate. The flame propagated vertically downward with an electric spark at the top of rod. Flame images were recorded using a camera (Nikon, D750). A blue LED was used as the backlight to obtain the position of the molten sphere in the blue image of the flame. A polarizing filter in front of the camera lens was used to diminish the flame chemiluminescence and back-

ground blue LED light. The flame spread rate was measured by tracking the flame base location and molten sphere position as a function of time. An image of the flame was captured using a digital camera (Figure 3a) and decomposed it into red, green,
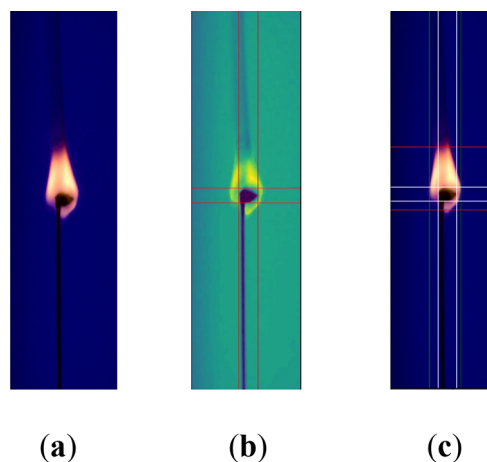

Figure 3. Flame shape and detection of the flame and the molten sphere: (a) raw photograph, (b) detection of the molten sphere within the flame in the blue image, and (c) detected flame base location and molten sphere position.

and blue channels using an in-house code. The blue channel image was used to determine the position of the molten sphere (Figure 3b), while the red channel image was used to extract the flame characteristics. The obtained flame length and the molten sphere's width and length are presented in Figure 3c.

2.2.6. Mechanical Property Measurement—Stiffness. The yield stress was measured using a push−pull gauge (DACELL FGA 20), as shown in Figure 4. An approximately 40 mm-long
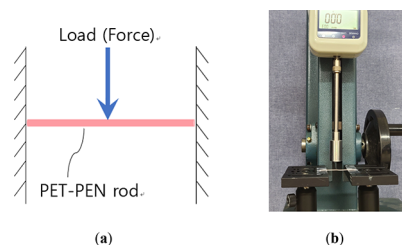

Figure 4. Yield stress experimental apparatus: (a) schematic and (b) push−pull gauge with a PET/PEN rod.

rod of PET−PEN was set horizontally, and each end of the rod was tightly fixed. The push−pull gauge slowly applies the load vertically at the center of the rod until the rod breaks apart. The yield stress was recorded at the break point.

3. RESULTS AND DISCUSSION

3.1. Microstructure. The quantity of CO_2 absorbed is a critical factor in physical foaming since it significantly affects the internal structure of the foam, including pore size and distribution. The foaming conditions were determined by conducting sorption tests.[17,22] As a fundamental-level investigation of one-step foaming, we used a pristine filament in a cylindrical microrod extruded through a nozzle with a diameter of 0.4 mm in a fused filament fabrication (FFF) 3D printer. A range of foaming temperatures from 225 to 235 °C were
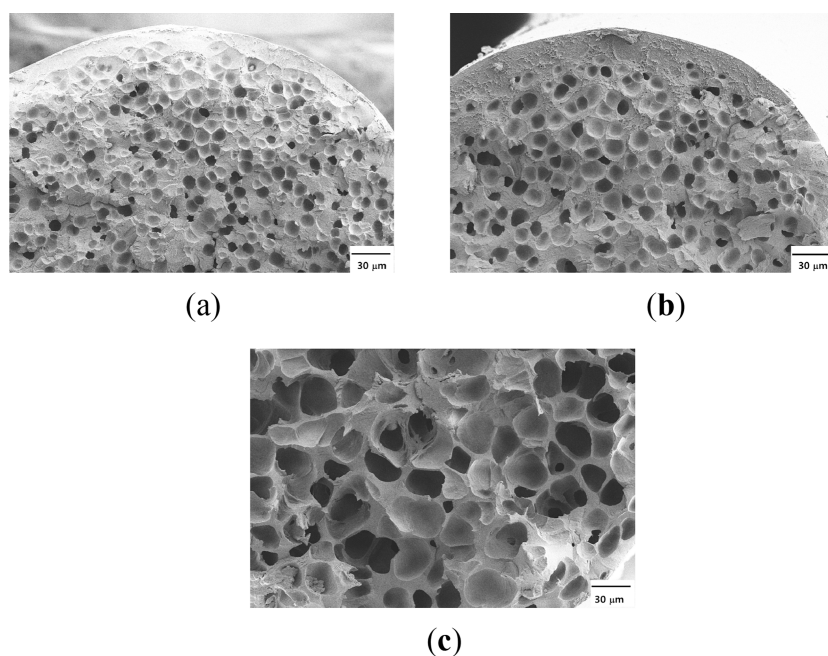
Figure 5. SEM micrographs of the foamed PET−PEN copolymer for T_f equal to (a) 225, (b) 230, and (c) 235 °C.

tested, and typical cross-sectional SEM images of the resulting foam are shown in Figure 5.

One-step foaming has been investigated in ref 17. Following rapid pressure relief, the nuclei of the polymer matrix begin to grow into pores according to the cell growth mechanism when the nucleus exceeds a critical value. The concentration gradient induces a foam gradient. Due to the CO_2 concentration in the microrod, the cells are uniformly grown, except near the surface. The underlying reason for this phenomenon is "gas escaping" near the wall. Therefore, the radius of nuclei near the wall does not exceed the critical value, and they fail to grow. Thus, the process of pore formation is suppressed. This is the mechanism for the formation of a dense skin layer near the outer boundary. However, the CO_2 concentration in the surface at 30 MPa and 235 °C exceeded the lower limit, and nuclei were thus able to grow into foams with a larger pore size.

To characterize the pore morphology, the interrogation area of the SEM image was examined over 100−240 μm squares depending on pore size. The measured pore size distributions are shown in Figure 6. Note that distributions of the pore size in one-step foaming are narrow compared to two-step foaming. It can be seen that the higher the foaming temperature, the larger the pore diameter. This is due to reduced viscosity of the polymer in nucleation and cell growth. In the case of a foaming temperature of 235 °C, there is a wider distribution and a slight increase in the outermost pore size due to a softer copolymer matrix at the elevated foaming temperature.

Figure 7 shows that the pore size distribution and probability density function were evaluated from the image analysis results. The number-averaged pore diameter, d_{pore}, was calculated. As the foaming temperature increases, there is a gradual increase in the average diameter, i.e., average diameters were 8.63, 12.87, and 25.75 μm at 225, 230, and 235 °C, respectively. The standard deviations obtained for 225, 230, and 235 °C were 3.06, 3.12, and 7.20 μm, respectively. There were differences in the mean diameter, as it was calculated not on an area-average but on a number-average basis.
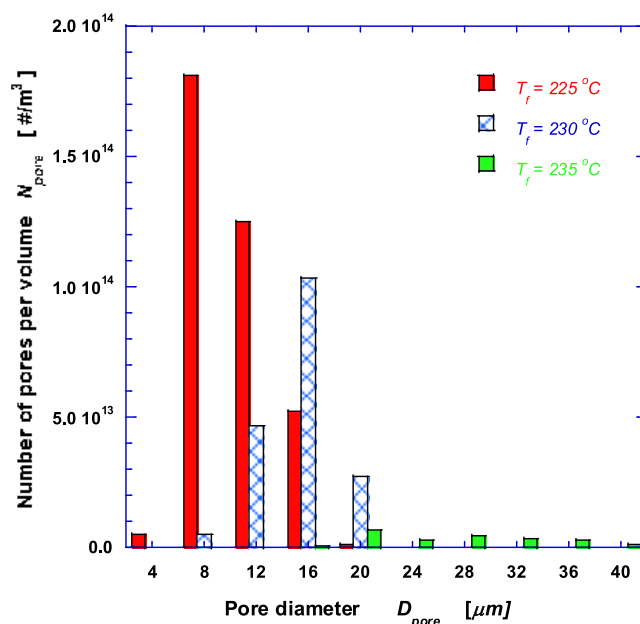

Figure 6. Number of pores per volume due to sorption temperature in one-step foaming of PET−PEN copolymer filaments.

Even though the PET−PEN rods were constructed through two different processes and various foaming temperatures, there was commonality in the density. The density was 1.419 mg/mm^3 for the raw material and 0.768 and 0.371 mg/mm^3 for the two-step PET−PEN at 40 and 100 °C, respectively. The density of the one-step PET−PEN was 1.277, 1.04, and 0.778 mg/mm^3 at 225, 230, and 235 °C, respectively. In addition, pores of larger size tended to be concentrated at higher foaming temperatures due to CO_2 being more saturated at higher T_f. It is acceptable that the density of both one-step and two-step PET−PEN is reduced as the foaming temperature increases.
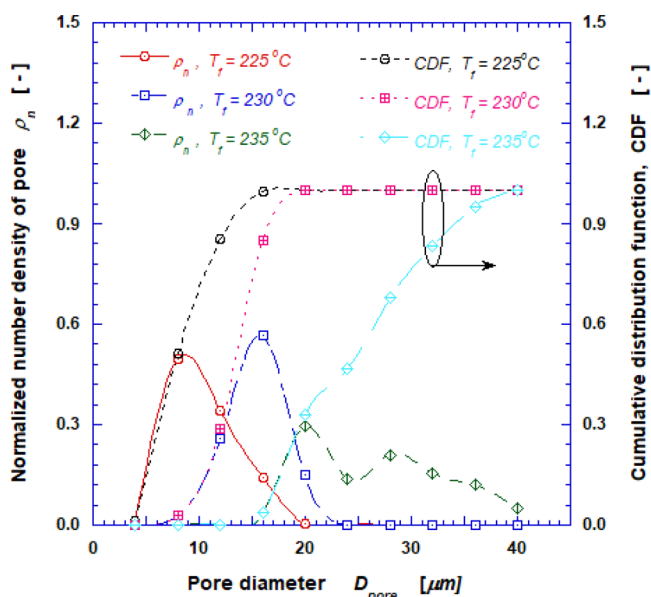
Figure 7. Size distribution of pores and probability density function for the CO_2-foamed PET−PEN structure (one-step foaming, sorption at 225−235 °C for 30 min) measured from SEM images.

3.2. Thermal History and Pyrolysis Analysis.

The second heating of the one-step foamed sample revealed an initial glass transition at approximately 72.9 °C for the raw material, as depicted in Figure 8a. The change near the glass transition temperature became less apparent as the foaming temperature was increased from 225 to 235 °C.

The crystalline melting process in the second heating cycle showed endothermic peaks at 238.4 °C. It was found to have no impact on the foaming temperature of the supercritical fluid. Thermal transitions observed in the temperature peak around 149.7−157.2 °C are related to cold crystallization, an endothermic process. Cold crystallization is caused by the rearrangement of molecular chains in the crystalline copolymer layer. The cold crystallization peak decreased with increasing foaming temperature due to chain relaxation and finally disappeared.

Pyrolysis measurements were performed using an SDT analyzer for the one-step foamed structures. From the pyrolysis curve shown in Figure 8b, it can be seen that the copolymer starts to evaporate near 350 °C and has a maximum weight loss of 76.9% at 438.4 °C (2.08 wt %/°C) for the foaming temperature of 235 °C. A major pyrolysis event takes place between 390 and 470 °C, where most of the latent heat of evaporation was consumed. The thermal decomposition rate of the foamed material increases rapidly to above about 360 °C, resulting in a large loss of mass, so the upper temperature limit of the 3D printing operation should be set sufficiently lower than 350 °C. Note that the nozzle temperature for fabricating the microrod in this study was 275 °C. There were also no significant differences between the foamed structures for the investigated conditions.

3.3. Mechanical Property—Stiffness.

The foaming process significantly influences the physical and mechanical properties of the PET−PEN rods, particularly their brittleness. The one-step PET−PEN samples were found to be more fragile and prone to breaking at the position where force was applied. However, the raw and two-step materials were stretched near the bonded sides of the rod before breaking. The stress at break or yield stress, S_b, was calculated according to the diameters and breaking forces of the strands. The S_b of the PET−PEN raw material was determined to be 70 MPa, which is comparable to the findings of Panowicz et al.[23] They reported that S_b for fresh (or as-received) PET at 25 °C was 82.7 MPa, and aging resulted in a decrease in S_b due to a larger crystalline phase and crosslinking between monomers.

Figure 9 illustrates the effect of foaming methods and foaming temperature on the yield stress. The trends reveal that
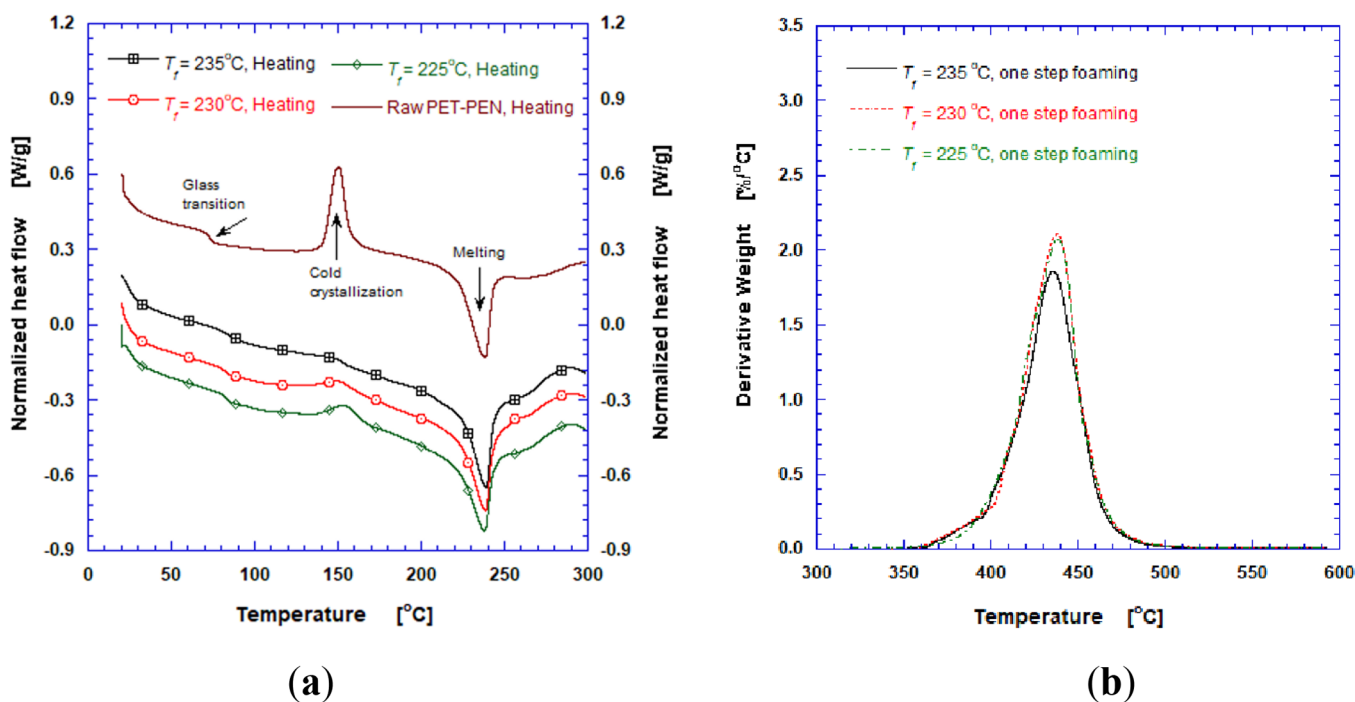

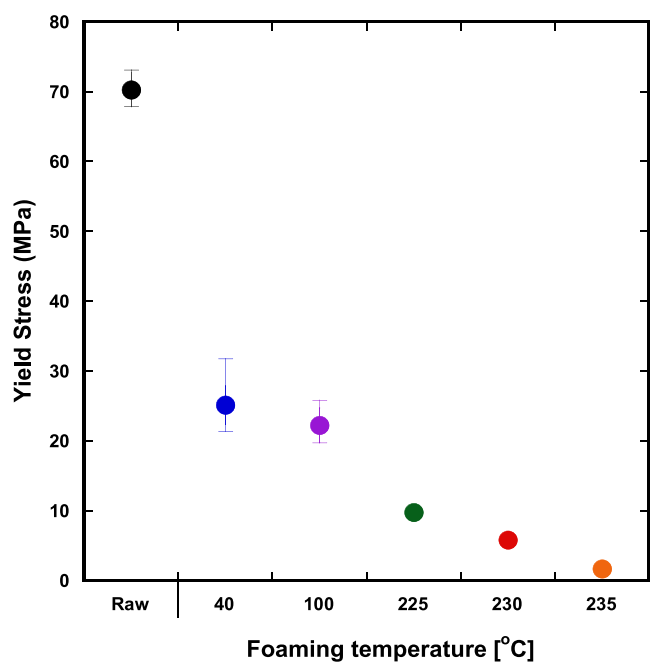**Figure 8.** (a) DSC and (b) TGA thermograms of the samples for the solid rod and foam grid.

Figure 9. Effect of foaming temperature on the yield stress (two-step foaming (T_f = 40 and 100 °C); one-step foaming (T_f = 225−235 °C)).

the yield stress decreases with increasing foaming temperature, with values of 9.5 MPa for T_f = 225 °C, 5.6 MPa for 230 °C, and 1.7 MPa for 235 °C. Notably, the yield stress for the one-step T_f = 235 °C case is only 2.4% of that for the raw material, indicating that it is more fragile.
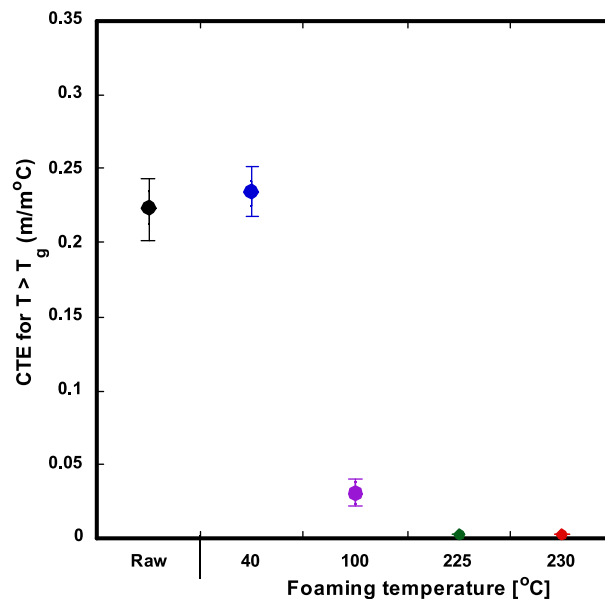
3.4. Thermal Expansion. The coefficient of thermal expansion was measured based on the slope of the PET−PEN rod length versus the ambient air temperature as in Figure 10a. Below 70 °C, all rods of two-step PET−PEN expanded slowly. The length of the rods increased relatively rapidly at a certain temperature, namely, the glass transition temperature. After exceeding the T_g, the coefficients of thermal expansion, i.e., the slopes of Figure 10a, were evaluated as 0.22, 0.23, and 0.031 mm/°C for the raw, 40 °C, and 100 °C cases, respectively. The foaming temperature of 40 °C is representative of the steep expansion group (SEG), and T_f = 100 °C is representative of the mild expansion group (MEG) of the two-step process with the raw material as a reference. Contrary to the two-step rods, there was a small change in the slope for the one-step rods. For the 235 °C cases, it was not possible to conduct the expansion experiment as the copolymer was too stiff and brittle, as described in Section 3.2. This prevented the rods from being straightened and hooked up into the inner tube of Figure 2 for the experiment. The coefficients of thermal expansion for T_f = 225 and 230 °C were 0.0023 and 0.0015 mm/°C, respectively, which are two orders of magnitude lower than that of the SEG (Figure 10b). These are classified as the low expansion group (LEG), as presented in Table 1.

3.5. Flame Spread Rate and Burned Length Rate. PET−PEN produces a yellowish flame with a slightly different shape depending on the T_f and postfoaming process.[1] Digital flame images can be decomposed into red, green, and blue components. Since soot in the flame emits yellow-orange light, the red component of the flame image is related to soot. The flame of the raw material was very weak and small and almost extinguished before the whole rod burned. For the raw material and for 40, 225, and 230 °C, the flame fragments scattered outward and burned, which resulted in irregular flame shapes. Figure 11 shows pseudocolor blue images of the flames. The blacker color represents a lower intensity, whereas the yellow represents a higher intensity. As the molten sphere blocked the blue LED backlight, it appears as black or dark blue. Though the diffusion flame did not illuminate the blue color, the flame
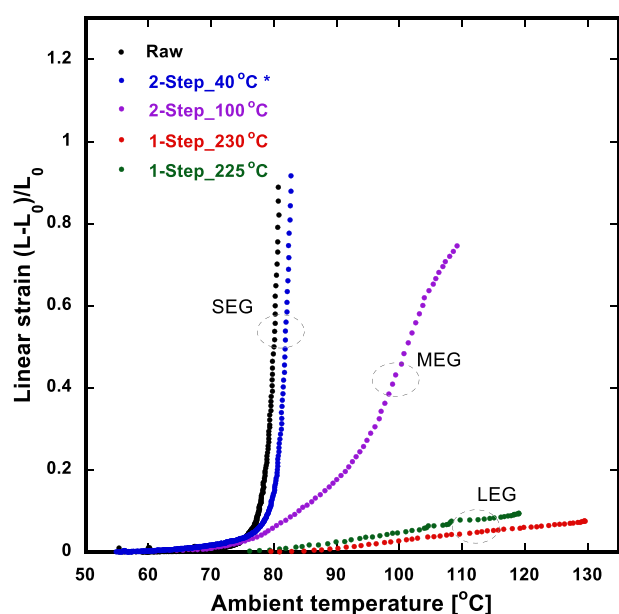
(a)

(b)

Figure 10. Behavior of the PET−PEN materials: (a) elongation of the rods due to the ambient air temperature change and (b) coefficient of thermal expansion.
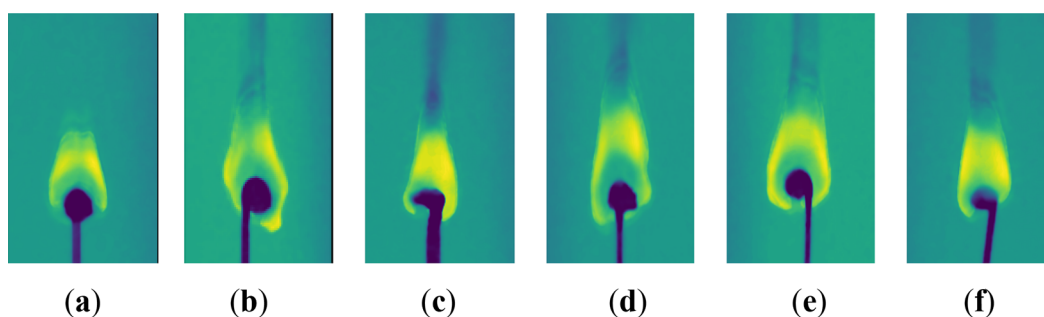
Figure 11. Pseudocolor blue images of the flames showing the flame and the molten sphere shapes. (a) Raw material and PET−PEN produced under the following conditions: (b) two-step with T_f = 40 °C, (c) two-step with T_f = 100 °C, (d) one-step with T_f = 225 °C, (e) one-step with T_f = 230 °C, and (f) one-step with T_f = 235 °C.

shapes appeared in the images as the CCD sensor in the camcorder perfectly filters blue light and the bright soot emitted a weak blue light by blackbody radiation. Smoke, which appears black, can be seen downstream of the flame because the smoke particles block the LED beam. For the SEG and one-step rods, relatively large molten spheres were suspended at the end of a rod bent downward in the flame. However, in the two-step 100 °C and one-step 235 °C cases, the molten polymers were relatively small, the burning rods less bent, and the flames appeared on the top of them. Thus, the flames were more stable at high T_f for both one- and two-step postfoaming processes.

The red component of the flame, which is the dominant flame color visible to the naked eyes, can be considered as the flame zone. The area of the red component of the flame, equivalent to the flame size, is depicted as a time series in Figure 12. The raw material exhibited a relatively small flame that diminished in size before extinguishing. Once the SEG flame reached a quasi-steady state, its size remained relatively constant. The MEG flame had the longest burning time and exhibited abrupt changes in the flame area. The size of the LEG flame was intermediate, falling between those of the SEG and MEG flames.
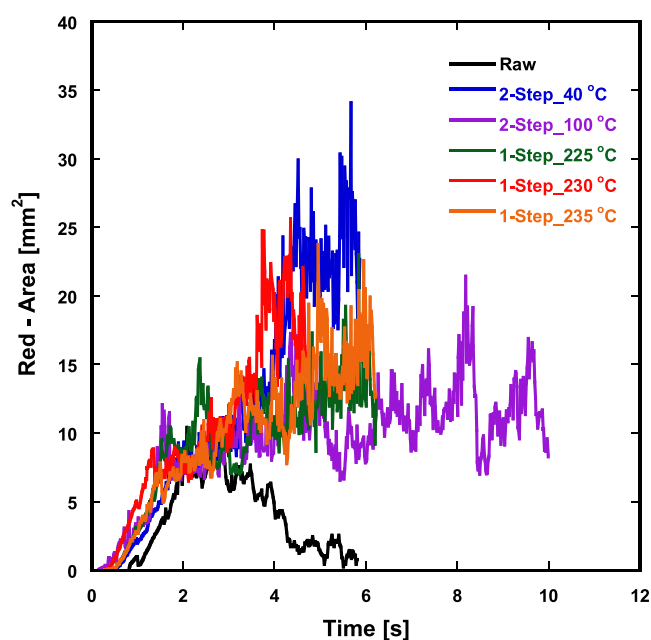

Figure 12. Temporal intensity changes in the red images of the flame.

As the rod was not straight, the melted part rotated slowly around the rod axis or bent from one direction to the other as it burned, which manifests as an unsmooth curve in Figure 13b, especially for the 100 °C case. The top of the rod before ignition was set at zero, vertically upward was a positive direction, and the moment when the arc filaments appeared on the video frame was set as 0 s. About 2 s after ignition, the flame developed, and the molten part grew with its increased movement. After that, it moved quasi-steadily. The shape and position of the diffusion flame depend on the fuel and oxygen mix, which is affected by the fluid dynamics of the fuel supplying part, buoyancy, and gravity. The movement of the molten sphere, the ejecting velocity of the volatile component of the PET−PEN from the molten part, and the external natural convective flow result in a complicated flame motion, as shown in Figure 13b. Flame edge tracking has been commonly used in combustion studies to measure the flame spread rates or flame propagation velocities of gaseous fuels,[24,25] electrical wire burning,[26,27] solid fuels,[28,29] and flame retardants.[30] The position of the flame base and the bottom of the molten sphere were measured to calculate the flame spread rate from the negative slope of the graphs in Figure 13 during the quasi-steady periods. As the differences in the flame spread rates, according to the measurement positions, were within 2%, the movement of the molten sphere base was hereafter considered as the flame spread rate.

Figure 14 shows that the SEG, i.e., T_f = 40 °C, had a higher flame spread rate than the MEG, i.e., T_f = 100 °C comparable to that of the LEG, i.e., the one-step foaming rods. The relatively large molten sphere and the high thermal elongation properties of the SEG are attributed to the bending of the heated rod and the higher flame spread rates among the two-step processing cases.[1]

The size or volume of the molten sphere of the one-step processing rods, larger than that of the MEG and smaller than that of the SEG, as shown in Figure 11, was not indicative of the trend of flame spread rates. The suspended unburned mass, i.e., the molten sphere of both the SEG and the LEG, was comparable given that the density of the one-step rods is higher than that of the two-step SEG, as seen in Figure 7. As the thermal expansion for the LEG is two orders of magnitude less than that for the SEG, as mentioned previously, the mass of the molten sphere alone cannot indicate the trends of flame spread rates. Other approaches are needed, which will be discussed later.

3.6. Unburned Mass Fraction. The solid PET−PEN rod burned after it was melted near or within the flame, as shown in Figure 11. During the combustion period, its length was
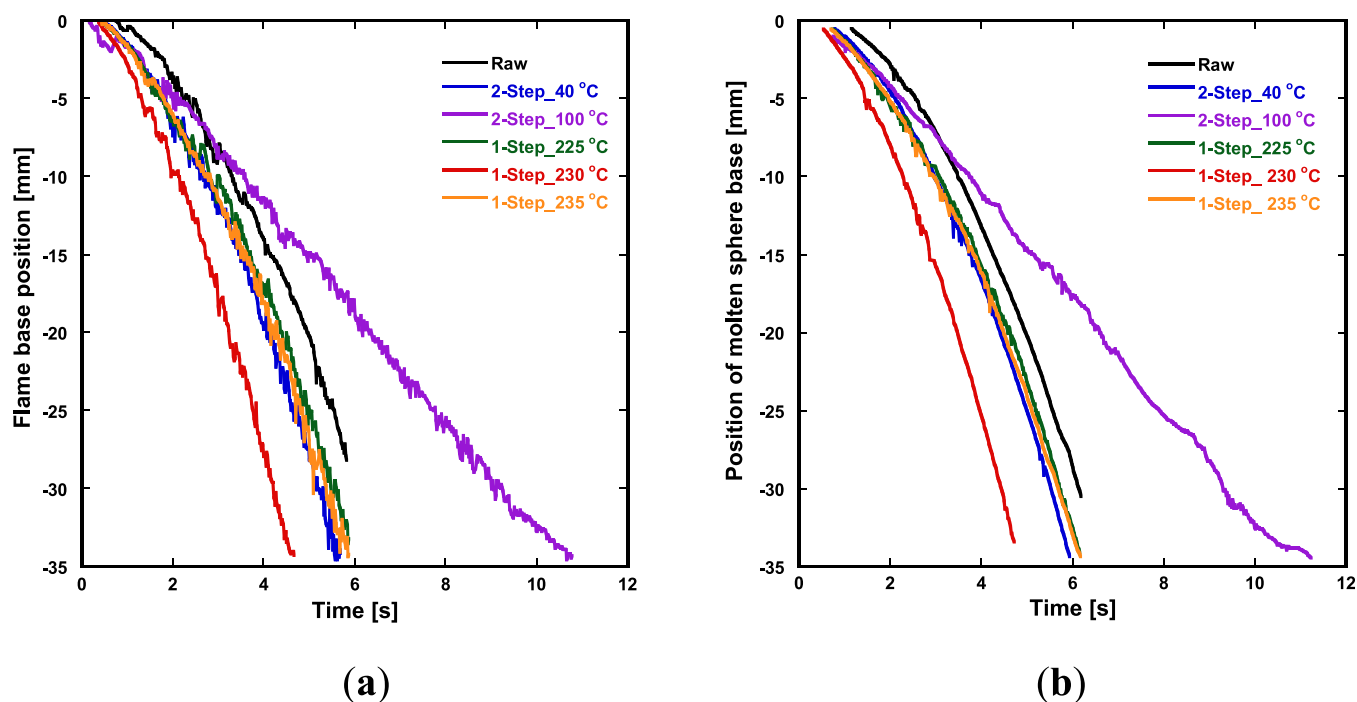
Figure 13. Movement of the flame evaluated by the position of (a) flame base and (b) bottom of the molten sphere.
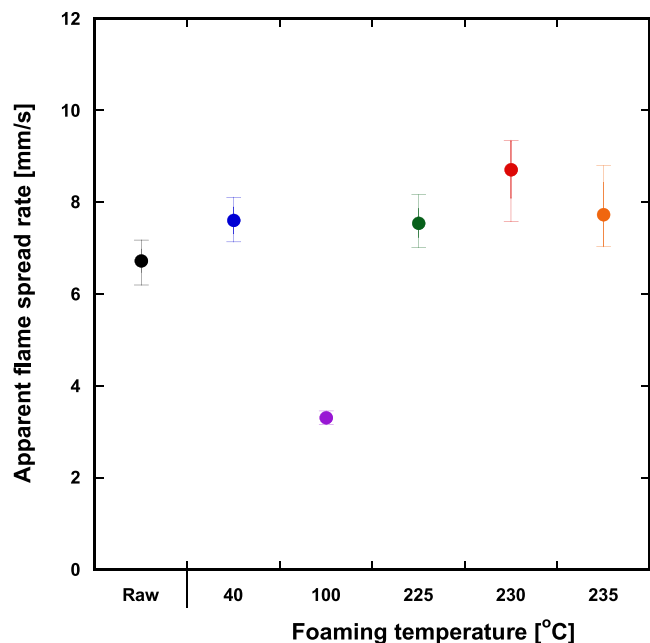

Figure 14. Foaming temperature effects on the apparent flame spread rate (two-step foaming (T_f = 40 and 100 °C); one-step foaming (T_f = 225−235 °C)).

Figure 15. Conceptual diagram of the rods: (a) initial rod, (b) rod while burning, and (c) conceptual rod for the burned and molten portions.

where subscript 0 denotes that of the initial fresh rod.

Although the unburned length, L_u, was reduced, the length of the rod was not all burnt due to the presence of a molten mass. The fraction of the remaining residue after flame extinction is a parameter that adequately indicates whether there is complete combustion or not. The burned mass fraction (Y_b) is defined as the actual burned mass divided by the apparent burned mass, which is the mass corresponding to the reduced length of the rod:

$$Y_b = \frac{m_b}{m_r} = \frac{m_b}{(m_b + m_m)} \quad (4)$$

The molten mass fraction (Y_m) is defined as

$$Y_m = 1 - Y_b \quad (5)$$

The burned mass fraction was evaluated by the measurement of the initial mass and length and those after the abrupt flame extinction for which a microprecision scale (Mettler Toledo, MX5, resolution of 0.001 mg) was used. Figure 16

reduced. However, a part of the rod burned completely, a part was converted to a molten sphere, and the other parts were not affected by the flame. Hereafter, they will be identified using subscripts, i.e., 0, r, b, m, and u for the initial rod and the reduced, burned, molten, and unaffected parts, respectively, as shown in Figure 15.

$$L_0 = L_b + L_m + L_u \quad (2)$$

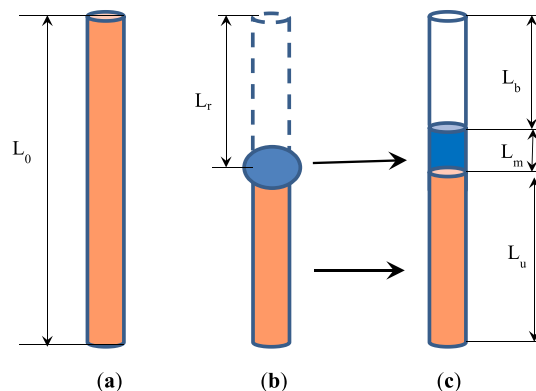The mass of the molten sphere is
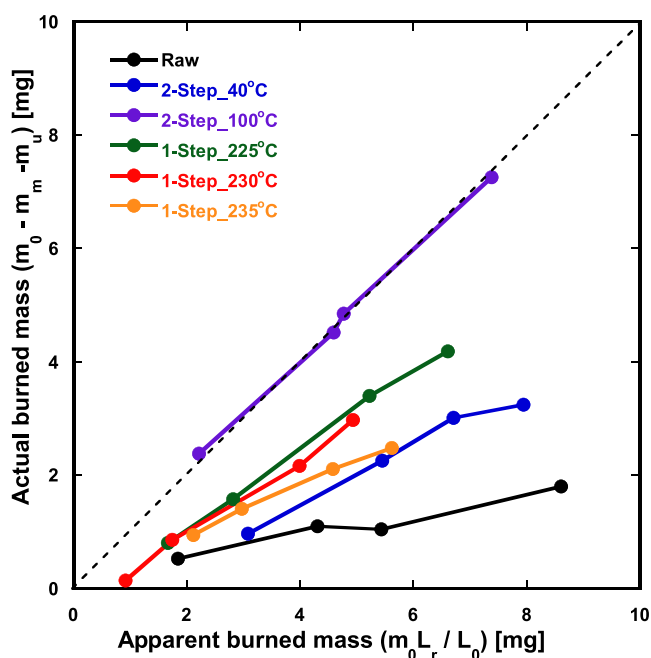
$$M_m = \rho_o A_0 L_m \quad (3)$$

Figure 16. Effect of foaming temperature and foaming methods on the actual and apparent burned mass.

Figure 17. Effect of foaming temperature on the molten mass fraction, which represents the fraction of the molten parts among the mass of the whole parts that have been affected by the flame.

shows the effects of the foaming temperature and the foaming steps on the apparent and actual burned mass. The apparent burned mass is equal to the actual burned mass if there is no molten portion, such as gaseous fuel combustion, which is presented as a dotted line. Therefore, the dotted line represents the apparent mass, m_a. Below each curve is the actual burned mass, m_b. The difference between the dotted line and each actual burned mass curve represents the mass of the molten sphere, m_m, or the residue if it is quenched quickly. The two-step MEG cases are located near the dotted line, indicating that the molten portion is small, as anticipated by the size of the molten sphere in Figure 11c. The raw material and two-step 40 °C cases, i.e., the SEG, had a large molten sphere during combustion. The one-step rod molten portion sizes are between those of the SEG and the MEG.

The molten mass fraction is equivalent to the remaining mass fraction as it is melted and will remain unburned if the sample is quenched abruptly. The foaming temperature and foaming methods affect the molten mass fraction greatly, as shown in Figure 17. While 76% of the reduced length of the raw material was unburned, this was only 1% in the case of the two-step 100 °C rod, i.e., the MEG. For the LEG, i.e., the one-step rods, 41−55% of the reduced mass will form a residue.

3.7. Actual Mass Burning Rate. The formation of hazardous and/or eco-unfriendly components, such as soot, NO_x, and dioxin, is related to actual mass burning. Due to the molten sphere, the actual mass burning rate is different from the apparent mass burning rate. The actual mass burning rate was obtained by

$$\dot{m}_b = \frac{dm_b}{dt} \approx \frac{\Delta m_b}{\Delta t} = \frac{\Delta m_b}{L_r/v_r} \tag{6}$$

where v_r is the apparent velocity of the flame obtained in Figure 14.

The raw material has a high apparent burning velocity as in Figure 14, but the actual burning rate is very low as shown in Figure 18 because the unburnt molten mass fraction is high as
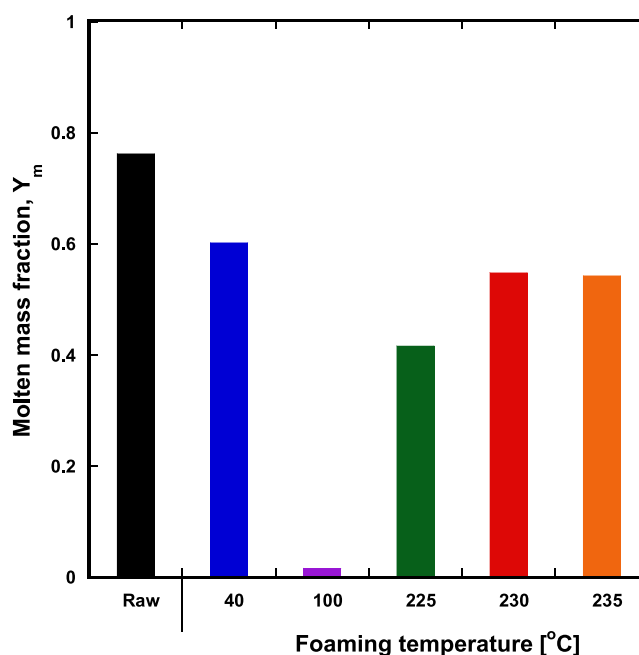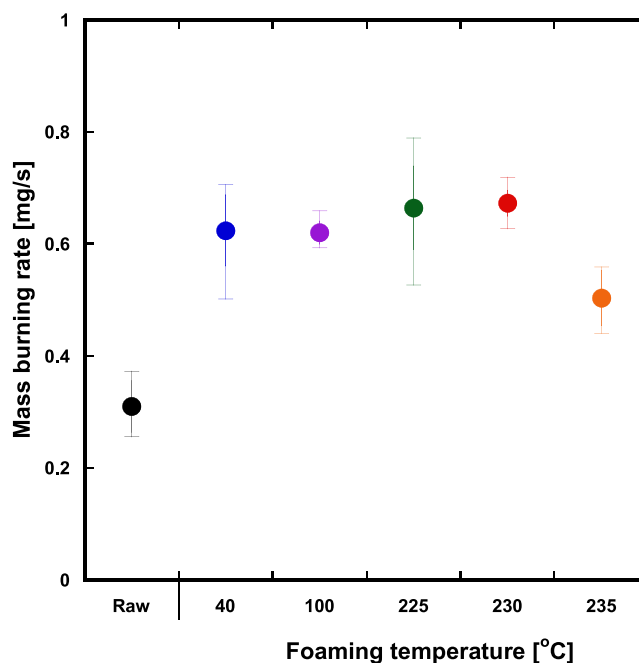

Figure 18. Effect of foaming temperature on the actual mass burning rate.

in Figure 17. The situation is the opposite for the MEG, i.e., a low apparent burning velocity but a smaller Y_m and, thus, a large actual mass burning rate. The actual mass burning rates for T_f = 40 °C and the LEG were in the range of 0.5−0.7 mg/s, as they had similar apparent burning velocities and molten mass fractions.

One-step PET−PEN has higher v_r, and the two-step MEG has a higher CTE. This is not the same trend as previous results studied using only two-step PET−PENs:[1] the higher the CTE, the higher the v_r. The obtained actual mass burning

rate was similar in both cases. This trend of the actual mass burning rate and the molten mass fraction explains why one-step cases have similar flame spread rates to the SEG cases: The flame of two-step MEG PET−PEN propagates slowly because it burns completely with little residue. The one-step PET−PEN flame propagates at a faster rate because it leaves a larger amount of unburned residue while achieving a similar actual burning mass per unit time.

4. CONCLUSIONS

Experimental investigation was conducted to examine the differences in thermal and mechanical properties, with a particular focus on combustion behavior, between PET−PEN copolymers prepared by one- and two-step processes.

With an increase in foaming temperature T_f, the brittleness of PET−PEN increased. The breaking stress of the one-step PET−PEN foamed at the highest T_f was only 2.4% of the raw material. Additionally, as T_f increased, the pore size of the foams increased, and the distribution became wider.

The coefficient of thermal expansion (CTE) of one-step PET−PEN was found to be approximately two orders of magnitude lower than that of the two-step SEG. Moreover, the melted mass fraction (Y_m), which is the ratio of the remaining residue mass to the mass corresponding to the volume of the material reduced by the flame, was 0.76 for the raw material, 0.01 for the two-step MEG, and between 0.41 and 0.55 for the one-step. The actual mass burning rates were comparable across all groups, except for the raw material. The trends in the actual mass burning rate and Y_m effectively accounted for the differences in flame speed among the groups.

■ AUTHOR INFORMATION

Corresponding Authors

Byeong Jun Lee − *School of Mechanical Engineering, Yeungnam University, Gyeongsan, Gyeongbuk 38541, Korea;* ⓞ orcid.org/0000-0002-0320-8195; Email: bjlee@yu.ac.kr

Byung Kyu Park − *Institute of Advanced Machines and Design, Seoul National University, Seoul 08826, Korea;* ⓞ orcid.org/0000-0002-3097-7715; Email: bkpark@snu.ac.kr

Author

Dong Hyeon Kim − *School of Mechanical Engineering, Yeungnam University, Gyeongsan, Gyeongbuk 38541, Korea;* ⓞ orcid.org/0009-0007-0810-6423

Complete contact information is available at:
https://pubs.acs.org/10.1021/acsomega.3c00810

Author Contributions

B.K.P. and B.J.L. performed conceptualization; D.H.K., B.K.P., and B.J.L. performed the methodologies, validation, and writing of the original draft; B.J.L. and D.H.K. performed analysis and review and editing of the manuscript; B.J.L. performed data curation; B.K.P. performed project administration and funding acquisition. All authors have read and agreed to the published version of the manuscript.

Notes

The authors declare no competing financial interest.

■ ACKNOWLEDGMENTS

■ REFERENCES

(1) Park, B. K.; Kim, C. J.; Lee, B. J. Effect of Foaming Temperature on Microstructure, Mechanical Properties and Flame Spread Rate in PET−PEN Copolymer. *Energies* **2021**, *14*, 957.

(2) Kausar, A. Polyurethane Composite Foams in High-Performance Applications: A Review. *Polym.-Plast. Technol. Eng.* **2018**, *57*, 346−369.

(3) Lee, D. I.; Ha, Y. H.; Jeon, H.; Kim, S. H. Preparation and Properties of Polyurethane Composite Foams with Silica-Based Fillers. *Appl. Sci.* **2022**, *12*, 7418.

(4) Zaidi, S. F. A.; Haq, E. U.; Nur, K.; Ejaz, N.; Anis-ur-Rehman, M.; Zubair, M.; Naveed, M. Synthesis & characterization of natural soil based inorganic polymer foam for thermal insulations. *Constr. Build. Mater.* **2017**, *157*, 994−1000.

(5) Gupta, N.; Zeltmann, S. E.; Shunmugasamy, V. C.; Pinisetty, D. Applications of polymer matrix syntactic foams. *JOM* **2014**, *66*, 245−254.

(6) Saint-Michel, F.; Chazeau, L.; Cavaillé, J. Y.; Chabert, E. Mechanical properties of high density polyurethane foams: I. Effect of the density. *Compos. Sci. Technol.* **2006**, *66*, 2700−2708.

(7) Galvagnini, F.; Valentini, F.; Dorigato, A. Development of polymeric insulating foams for low-temperature thermal energy storage applications. *J. Appl. Polym. Sci.* **2022**, *139*, No. e52397.

(8) Vatankhah, E.; Abasnezhad, M.; Nazerian, M.; Barmar, M.; Partovinia, A. Thermal energy storage and mechanical performance of composites of rigid polyurethane foam and phase change material prepared by one-shot synthesis method. *J. Polym. Res.* **2022**, *29*, 81.

(9) Galvagnini, F.; Dorigato, A.; Valentini, F.; Fiore, V.; la Gennusa, M.; Pegoretti, A. Multifunctional polyurethane foams with thermal energy storage/release capability. *J. Therm. Anal. Calorim.* **2022**, *147*, 297−313.

(10) Sobolčiak, P.; Mrlik, M.; Popelka, A.; Minařík, A.; Ilcikova, M.; Srnec, P.; Nogellova, Z.; Ouederni, M.; Krupa, I. Foamed Phase Change Materials Based on Recycled Polyethylene/Paraffin Wax Blends. *Polymer* **2021**, *13*, 1987.

(11) Ansari, M. A.; Somdee, P. Piezoelectric Polymeric Foams as Flexible Energy Harvesters: A Review. *Adv. Energy Sustainability Res.* **2022**, *3*, 2200063.

(12) Petroff, C. A.; Bina, T. F.; Hutchison, G. R. Highly Tunable Molecularly Doped Flexible Poly(dimethylsiloxane) Foam Piezoelectric Energy Harvesters. *ACS Appl. Energy Mater.* **2019**, *2*, 6484−6489.

(13) Zhang, W.; You, L.; Meng, X.; Wang, B.; Lin, D. Recent Advances on Conducting Polymers Based Nanogenerators for Energy Harvesting. *Micromachines* **2021**, *12*, 1308.

(14) Wendels, S.; Avérous, L. Biobased polyurethanes for biomedical applications. *Bioact. Mater.* **2021**, *6*, 1083−1106.

(15) Du, C. L.; Liu, J. Y.; Fikhman, D. A.; Shi, D. K.; Monroe, M. B. B. Shape Memory Polymer Foams With Phenolic Acid-Based Antioxidant and Antimicrobial Properties for Traumatic Wound Healing. *Frontiers in Bioengineering and Biotechnology* **2022**, *10*, DOI: 10.3389/fbioe.2022.809361.

(16) Jang, L. K.; Fletcher, G. K.; Monroe, M. B. B.; Maitland, D. J. Biodegradable shape memory polymer foams with appropriate thermal properties for hemostatic applications. *J. Biomed. Mater. Res., Part A* **2020**, *108*, 1281−1294.

(17) Kwon, D. E.; Aregay, M.G.; Park, B.K.; Lee, Y.W. *Preparation of polyethylene terephthalate foams at different saturation temperatures using dual methods of supercritical batch foaming.* 2021

(18) Tonelli, A. E. PET versus PEN: what difference can a ring make? *Polymer* **2002**, *43*, 637−642.

(19) Pulido, B. A.; Habboub, O. S.; Aristizabal, S. L.; Szekely, G.; Nunes, S. P. Recycled Poly(ethylene terephthalate) for High

Temperature Solvent Resistant Membranes. *ACS Appl. Polym. Mater.* **2019**, *1*, 2379−2387.

(20) Okolieocha, C.; Raps, D.; Subramaniam, K.; Altstdt, V. Microcellular to nanocellular polymer foams: Progress (2004-2015) and future directions. *Eur. Polym. J.* **2015**, *73*, 500−519.

(21) Tetlow, D.; de Simon, L.; Liew, S. Y.; Hewakandamby, B.; Mack, D.; Thielemans, W.; Riffat, S. Cellulosic-crystals as a fumed-silica substitute in vacuum insulated panel technology used in building construction and retrofit applications. *Energy Build.* **2017**, *156*, 187−196.

(22) Park, B. K.; Kim, C.-J.; Kwon, D. E.; Lee, Y.-W. Design and Fabrication of of Partially Foamed Grid Structure Using Additive Manufacturing and Solid State Foaming. *Processes* **2020**, *8*, 1594.

(23) Panowicz, R.; Konarzewski, M.; Durejko, T.; Szala, M.; Łazinska, M.; Czerwinska, M.; Prasuła, P. Properties of Polyethylene Terephthalate (PET) after Thermo-Oxidative Aging. *Materials* **2021**, *14*, 3833.

(24) Wu, Y.; Wen, X. P.; Guo, Z. D.; Zhang, S.; Deng, H. X.; Wang, F. H. Experimental study on the propagation char-acteristics of hydrogen/methane/air premixed flames in a narrow channel. *Int. J. Hydrogen Energy* **2022**, *47*, 6377−6387.

(25) Cheng, Y. F.; Meng, X. R.; Ma, H. H.; Liu, S. H.; Wang, Q.; Shu, C. M.; Shen, Z. W.; Liu, W. J.; Song, S. X.; Hua, F. Flame propagation behaviors and influential factors of TiH2 dust explosions at a constant pres-sure. *Int. J. Hydrogen Energy* **2018**, *43*, 16355−16363.

(26) Park, S. H.; Kang, M. S.; Cha, M. S.; Park, J.; Chung, S. H. Flame spread over twin electrical wires with applied DC electric fields. *Combust. Flame* **2019**, *210*, 350−359.

(27) Kang, M. S.; Park, J.; Chung, S. H.; Yoo, C. S. Effect of the thickness of polyethylene insulation on flame spread over electrical wire with Cu-core under AC electric fields. *Combust. Flame* **2022**, *240*, No. 112017.

(28) Jun, J. Y.; Lee, B. J.; Song, D. J. Measurement of burning velocity for bare strand casted with a frozen mixture of nano/micro-aluminum particles and water. *J. Mech. Sci. Technol.* **2016**, *30*, 2409−2413.

(29) Bhattacharjee, S.; Carmignani, L.; Celniker, G.; Rhoades, B. Measurement of instantaneous flame spread rate over solid fuels using image analysis. *Fire Safety J.* **2017**, *91*, 123−129.

(30) Muhammad, F.; Sipponen, M. H.; Seppälä, A.; Österberg, M. Eco-friendly Flame-Retardant Cellulose Nanofibril Aerogels by Incorporating Sodium Bicarbonate. *ACS Appl. Mater. Interfaces* **2018**, *10*, 27407−27415.